

Multiple-relaxation-time lattice Boltzmann method for immiscible fluids at high Reynolds numbers

Abbas Fakhari and Taehun Lee*

Department of Mechanical Engineering, City College of City University of New York, New York, 10031, USA

(Received 2 November 2012; published 15 February 2013)

The lattice Boltzmann method for immiscible multiphase flows with large density ratio is extended to high Reynolds number flows using a multiple-relaxation-time (MRT) collision operator, and its stability and accuracy are assessed by simulating the Kelvin-Helmholtz instability. The MRT model is successful at damping high-frequency oscillations in the kinetic energy emerging from traveling waves generated by the inclusion of curvature. Numerical results are shown to be in good agreement with prior studies using adaptive mesh refinement techniques applied to the Navier-Stokes equations. Effects of viscosity and surface tension, as well as density ratio, are investigated in terms of the Reynolds and Weber numbers. It is shown that increasing the Reynolds number results in a more chaotic interface evolution and eventually shattering of the interface, while surface tension is shown to have a stabilizing effect.

DOI: [10.1103/PhysRevE.87.023304](https://doi.org/10.1103/PhysRevE.87.023304)

PACS number(s): 02.70.-c, 02.60.Cb, 47.11.-j

I. INTRODUCTION

Among many classical multiphase fluid flow problems, instability of a shear layer, also known as Kelvin-Helmholtz instability (KHI) [1], is one of the most interesting and challenging subjects in that the interface undergoes a complex evolution and even a breakup depending, mostly, on the Reynolds and Weber numbers. This phenomenon is of fundamental importance in studying turbulent mixing layers and chemically reacting flows. Needless to say, fully understanding the mechanisms behind the breakup of an interface between two immiscible fluids is crucial in the study of atomization and fuel injection processes.

In the past decades, numerous authors have studied the shear-layer instability at the interface of a two-phase system [2–14]. Most of the published works dealt with two miscible fluids or two immiscible fluids with equal density, and a few works have been carried out for instability dynamics of two immiscible fluids with a density contrast. Rangel and Sirignano [6] used a vortex discretization approach to study the effects of density ratio and surface tension on the evolution of small disturbances at the interface between two inviscid, immiscible fluids neglecting gravitational force in a two-dimensional (2D) domain. They showed that increasing either surface tension or density ratio decreases the growth of disturbances. Using a front-tracking technique, Tauber *et al.* [11] investigated the effects of Reynolds and Weber numbers on the behavior of two immiscible fluids with a sheared interface at density ratios of 1 and 10. Their results showed the generation of fingers of interpenetrating fluids at high enough Reynolds and relatively low Weber numbers. Cenicerros and Roma [12] studied the long-time dynamics of two immiscible fluids in a 2D shear layer using a fully adaptive mesh refinement (AMR) technique based on the immersed boundary method. They examined the evolution of the interface caused by a vortex sheet at high Reynolds numbers for the case of density- and viscosity-matched fluids in the presence of surface tension. In a recent study, the stability of a two-phase fluid in a temporally evolving mixing layer was examined by Fontane and Joly [13]

in both 2D and 3D using an AMR procedure. In their study, effects of surface tension and gravity were neglected and the effect of density variation on the evolution of the interface between two miscible fluids was considered at a fixed Reynolds number of 1500. More recently, Shadloo and Yildiz [14] considered the KHI of an inviscid, immiscible fluid using smoothed particle hydrodynamics (SPH), and they examined the effects of density variation across the shear layer.

In this study, we invoke the lattice Boltzmann method (LBM) [15,16] to study the instability of a shear layer at high Reynolds numbers. Zhang *et al.* [17] applied the kinetic-based LBM [18,19] with the Bhatnagar-Gross-Krook (BGK) collision model [20,21] to study the KHI of a density-matched fluid and reported that their results are in good agreement with those of Moser and Rogers [8]. Their simulations, however, were limited to low-Reynolds-number flows ($Re = 250$) due to the well-known numerical instability of BGK models at low relaxation times (or high Reynolds numbers). We incorporate the multiple-relaxation-time (MRT) collision model [22] into the recently proposed two-phase LBM for immiscible fluids at high density ratio [23] in an effort to enhance the numerical stability *at higher Reynolds numbers*.

After comparing the accuracy and stability of the BGK and MRT models, we will conduct the simulations of the KHI for two immiscible fluids at high Reynolds numbers with a density contrast. We will further evaluate the validity and accuracy of the proposed MRT method by comparing our findings with those based on an accurate AMR technique used in [12,13].

II. MRT-LBM FOR IMMISCIBLE FLOWS

To obtain the lattice Boltzmann equation for the evolution of pressure and momentum, we start from the discrete Boltzmann equation with a generalized collision operator Λ and the intermolecular force \mathbf{F} [18]:

$$\frac{Df_\alpha}{Dt} = \frac{\partial f_\alpha}{\partial t} + \mathbf{e}_\alpha \cdot \nabla f_\alpha = -\Lambda(f_\alpha - f_\alpha^{\text{eq}}) + \frac{(\mathbf{e}_\alpha - \mathbf{u}) \cdot \mathbf{F}}{c_s^2} \Gamma_\alpha, \quad (1)$$

where f_α is the particle distribution function, t stands for time, \mathbf{e}_α is the microscopic velocity set, \mathbf{u} is the macroscopic

*thlee@ccny.cuny.edu; <https://sites.google.com/site/leecny>

velocity, c_s is the lattice speed of sound, and

$$\Gamma_\alpha = w_\alpha \left[1 + \frac{(\mathbf{e}_\alpha \cdot \mathbf{u})}{c_s^2} + \frac{(\mathbf{e}_\alpha \cdot \mathbf{u})^2}{2c_s^4} - \frac{(\mathbf{u} \cdot \mathbf{u})}{2c_s^2} \right], \quad (2)$$

with w_α being the weight coefficient set [15,21]. The equilibrium distribution function is $f_\alpha^{\text{eq}} = \rho \Gamma_\alpha$. Note that in the BGK model [20,21], the relaxation operator Λ becomes a diagonal matrix.

We consider a two-dimensional nine-velocity model (D2Q9) with the velocity set given by $\mathbf{e}_\alpha = (0,0)$ for $\alpha = 0$; $\mathbf{e}_\alpha = (\cos \theta_\alpha, \sin \theta_\alpha)$ for $\alpha = 1-4$; and $\mathbf{e}_\alpha = \sqrt{2}(\cos \theta_\alpha, \sin \theta_\alpha)$ for $\alpha = 5-8$. The intermolecular forcing \mathbf{F} is given by (see [23] for details)

$$\mathbf{F} = -\nabla(p - \rho c_s^2) - C \nabla \mu, \quad (3)$$

in which p is the hydrodynamic pressure, ρ is the density, and C is the concentration. The definitions for the pressure, the concentration, and the macroscopic velocity using the particle distribution functions can be found later in this section [see Eqs. (25)–(28)]. For the present model, the chemical potential μ is explicitly given by

$$\mu = 4\beta C(C-1)(C-0.5) - \kappa \nabla^2 C, \quad (4)$$

where the parameters β and κ are related to the surface tension γ and interface width ξ by $\beta = 12\gamma/\xi$ and $\kappa = 12\gamma\xi/8$. Also, the concentration profile along the direction normal to a flat interface z is given by

$$C(z) = \frac{1}{2} \left[1 + \tanh \left(\frac{2z}{\xi} \right) \right]. \quad (5)$$

As is discussed in [19,23,24], introducing a new distribution function

$$g_\alpha = f_\alpha c_s^2 + (p - \rho c_s^2) w_\alpha, \quad (6)$$

and substituting it into the discrete Boltzmann equation, Eq. (1), results in

$$\begin{aligned} \frac{Dg_\alpha}{Dt} &= -\Lambda(g_\alpha - g_\alpha^{\text{eq}}) + (\mathbf{e}_\alpha - \mathbf{u}) \\ &\cdot [(\Gamma_\alpha - w_\alpha) \nabla \rho c_s^2 - \Gamma_\alpha C \nabla \mu]. \end{aligned} \quad (7)$$

Since we are interested in the incompressible limit or low Mach number flows ($\text{Ma} \ll 1$), the terms corresponding to $\mathbf{u} \cdot \nabla p$, which is of $O(\text{Ma}^3)$, are dropped from the above equation. Application of the trapezoidal rule in the integration of Eq. (7) leads to

$$\begin{aligned} g_\alpha(\mathbf{x} + \mathbf{e}_\alpha \delta_t, t + \delta_t) &= g_\alpha(\mathbf{x}, t) - \frac{1}{2} \mathbf{S}(g_\alpha - g_\alpha^{\text{eq}})|_{(\mathbf{x}, t)} - \frac{1}{2} \mathbf{S}(g_\alpha - g_\alpha^{\text{eq}})|_{(\mathbf{x} + \mathbf{e}_\alpha \delta_t, t + \delta_t)} \\ &+ \frac{\delta_t}{2} (\mathbf{e}_\alpha - \mathbf{u}) \cdot [(\Gamma_\alpha - w_\alpha) \nabla^B \rho c_s^2 - \Gamma_\alpha C \nabla^B \mu]_{(\mathbf{x}, t)} \\ &+ \frac{\delta_t}{2} (\mathbf{e}_\alpha - \mathbf{u}) \cdot [(\Gamma_\alpha - w_\alpha) \nabla^C \rho c_s^2 - \Gamma_\alpha C \nabla^C \mu]_{(\mathbf{x} + \mathbf{e}_\alpha \delta_t, t + \delta_t)}, \end{aligned} \quad (8)$$

where $\mathbf{S} = \delta_t \Lambda$. The superscripts C and B on the gradient operators stand for central and biased finite differences,

respectively, and they are expressed by [23,24]

$$\begin{aligned} \delta_t \mathbf{e}_\alpha \cdot \nabla^C \rho|_x &= \frac{\rho(\mathbf{x} + \mathbf{e}_\alpha \delta_t) - \rho(\mathbf{x} - \mathbf{e}_\alpha \delta_t)}{2}, \\ \delta_t \mathbf{e}_\alpha \cdot \nabla^B \rho|_x &= \frac{-\rho(\mathbf{x} + 2\mathbf{e}_\alpha \delta_t) + 4\rho(\mathbf{x} + \mathbf{e}_\alpha \delta_t) - 3\rho(\mathbf{x})}{2}. \end{aligned} \quad (9)$$

In order to maintain an explicit scheme, the following modified particle distribution function is introduced [23]:

$$\begin{aligned} \bar{g}_\alpha &= g_\alpha + \frac{1}{2} \mathbf{S}(g_\alpha - g_\alpha^{\text{eq}}) - \frac{\delta_t}{2} (\mathbf{e}_\alpha - \mathbf{u}) \\ &\cdot [(\Gamma_\alpha - w_\alpha) \nabla^C \rho c_s^2 - \Gamma_\alpha C \nabla^C \mu]. \end{aligned} \quad (10)$$

Then the modified equilibrium distribution function would be

$$\bar{g}_\alpha^{\text{eq}} = g_\alpha^{\text{eq}} - \frac{\delta_t}{2} (\mathbf{e}_\alpha - \mathbf{u}) \cdot [(\Gamma_\alpha - w_\alpha) \nabla^C \rho c_s^2 - \Gamma_\alpha C \nabla^C \mu]. \quad (11)$$

From the above relations, one can infer

$$\bar{g}_\alpha - \bar{g}_\alpha^{\text{eq}} = (\mathbf{I} + \frac{1}{2} \mathbf{S})(g_\alpha - g_\alpha^{\text{eq}}), \quad (12)$$

where \mathbf{I} is the identity matrix. Using the above relations, Eq. (8) can be recast as

$$\begin{aligned} \bar{g}_\alpha(\mathbf{x} + \mathbf{e}_\alpha \delta_t, t + \delta_t) &= \bar{g}_\alpha(\mathbf{x}, t) - (\mathbf{S} + 2\mathbf{I})(\bar{g}_\alpha - \bar{g}_\alpha^{\text{eq}})|_{(\mathbf{x}, t)} \\ &+ \delta_t (\mathbf{e}_\alpha - \mathbf{u}) \cdot [(\Gamma_\alpha - w_\alpha) \nabla^M \rho c_s^2 - \Gamma_\alpha C \nabla^M \mu]_{(\mathbf{x}, t)}, \end{aligned} \quad (13)$$

where the mixed difference is $\nabla^M = (\nabla^C + \nabla^B)/2$.

As proposed by Lallemand and Luo [22], the collision operator can be considered as

$$\mathbf{S} + 2\mathbf{I} = \mathbf{M}^{-1} \hat{\mathbf{S}} \mathbf{M}, \quad (14)$$

where the orthogonal transformation matrix and its inverse are given by

$$\mathbf{M} = \begin{bmatrix} 1 & 1 & 1 & 1 & 1 & 1 & 1 & 1 & 1 \\ -4 & -1 & -1 & -1 & -1 & 2 & 2 & 2 & 2 \\ 4 & -2 & -2 & -2 & -2 & 1 & 1 & 1 & 1 \\ 0 & 1 & 0 & -1 & 0 & 1 & -1 & -1 & 1 \\ 0 & -2 & 0 & 2 & 0 & 1 & -1 & -1 & 1 \\ 0 & 0 & 1 & 0 & -1 & 1 & 1 & -1 & -1 \\ 0 & 0 & -2 & 0 & 2 & 1 & 1 & -1 & -1 \\ 0 & 1 & -1 & 1 & -1 & 0 & 0 & 0 & 0 \\ 0 & 0 & 0 & 0 & 0 & 1 & -1 & 1 & -1 \end{bmatrix}, \quad (15)$$

and

$$\mathbf{M}^{-1} = \frac{1}{36} \begin{bmatrix} 4 & -4 & 4 & 0 & 0 & 0 & 0 & 0 & 0 \\ 4 & -1 & -2 & 6 & -6 & 0 & 0 & 9 & 0 \\ 4 & -1 & -2 & 0 & 0 & 6 & -6 & -9 & 0 \\ 4 & -1 & -2 & -6 & 6 & 0 & 0 & 9 & 0 \\ 4 & -1 & -2 & 0 & 0 & -6 & 6 & -9 & 0 \\ 4 & 2 & 1 & 6 & 3 & 6 & 3 & 0 & 9 \\ 4 & 2 & 1 & -6 & -3 & 6 & 3 & 0 & -9 \\ 4 & 2 & 1 & -6 & -3 & -6 & -3 & 0 & 9 \\ 4 & 2 & 1 & 6 & 3 & -6 & -3 & 0 & -9 \end{bmatrix}. \quad (16)$$

The diagonal relaxation matrix is then

$$\hat{\mathbf{S}} = \mathbf{M}(\mathbf{S} + 2\mathbf{I})\mathbf{M}^{-1} = \text{diag}(s_1, s_2, s_3, s_4, s_5, s_6, s_7, s_8, s_9). \quad (17)$$

The transformation matrix is constructed by orthogonalization of the discrete velocity set as is discussed in [22]. The rows of the transformation matrix are the following moments in 2D:

$$\mathbf{M} \equiv (|p\rangle, |e\rangle, |\epsilon\rangle, |j_x\rangle, |q_x\rangle, |j_y\rangle, |q_y\rangle, |\sigma_{xx}\rangle, |\sigma_{xy}\rangle)^T, \quad (18)$$

where

$$|p\rangle_\alpha = |\mathbf{e}_\alpha|^0 = 1, \quad (19a)$$

$$|e\rangle_\alpha = -4|\mathbf{e}_\alpha|^0 + 3(e_{\alpha,x}^2 + e_{\alpha,y}^2), \quad (19b)$$

$$|\epsilon\rangle_\alpha = 4|\mathbf{e}_\alpha|^0 - \frac{21}{2}(e_{\alpha,x}^2 + e_{\alpha,y}^2) + \frac{9}{2}(e_{\alpha,x}^2 + e_{\alpha,y}^2)^2, \quad (19c)$$

$$|j_x\rangle_\alpha = e_{\alpha,x}, \quad (19d)$$

$$|q_x\rangle_\alpha = [-5|\mathbf{e}_\alpha|^0 + 3(e_{\alpha,x}^2 + e_{\alpha,y}^2)]e_{\alpha,x}, \quad (19e)$$

$$|j_y\rangle_\alpha = e_{\alpha,y}, \quad (19f)$$

$$|q_y\rangle_\alpha = [-5|\mathbf{e}_\alpha|^0 + 3(e_{\alpha,x}^2 + e_{\alpha,y}^2)]e_{\alpha,y}, \quad (19g)$$

$$|\sigma_{xx}\rangle_\alpha = e_{\alpha,x}^2 - e_{\alpha,y}^2, \quad (19h)$$

$$|\sigma_{xy}\rangle_\alpha = e_{\alpha,x}e_{\alpha,y}. \quad (19i)$$

It is worth noting that there are several differences between the present MRT and the prior MRT models for multiphase flows [25–27]. One distinct feature of the present MRT model is that the generalized relaxation matrix is multiplied by the nonequilibrium part of the modified distribution function, as in the MRT-LBM for single-phase flows [22], but not by the forcing term, and there is no need to switch between phase and moment spaces. As a result, the implementation of the present MRT model becomes straightforward. Another key feature is that the relaxation rates for conserved quantities, namely, s_1, s_4, s_6 , can be set equal to zero without causing any numerical difficulties. This is in contrast to the other MRT implementations [25,26], in which these relaxation rates should be set to 1 due to the multiplication of the forcing term by the relaxation matrix and shifting back and forth between moment and phase spaces.

Now, in order to recover the advective Cahn-Hilliard equation [28], we utilize the LBM formulation proposed by

Lee and Liu [23]:

$$\begin{aligned} & \bar{h}_\alpha(\mathbf{x} + \mathbf{e}_\alpha \delta_t, t + \delta_t) \\ &= \bar{h}_\alpha^{\text{eq}}(\mathbf{x}, t) + \frac{\delta_t}{2} \Gamma_\alpha M \nabla^2 \mu|_{(\mathbf{x} + \mathbf{e}_\alpha \delta_t, t)} + \frac{\delta_t}{2} \Gamma_\alpha M \nabla^2 \mu|_{(\mathbf{x}, t)} \\ &+ \delta_t \Gamma_\alpha (\mathbf{e}_\alpha - \mathbf{u}) \cdot \left[\nabla^M C - \frac{C}{\rho c_s^2} (\nabla^M p + C \nabla^M \mu) \right]_{(\mathbf{x}, t)}, \end{aligned} \quad (20)$$

where M is the constant mobility and \bar{h}_α is the modified particle distribution function for the interface tracking equation,

$$\begin{aligned} \bar{h}_\alpha^{\text{eq}} &= C \Gamma_\alpha - \frac{\delta_t}{2} \Gamma_\alpha (\mathbf{e}_\alpha - \mathbf{u}) \\ &\cdot \left[\nabla^C C - \frac{C}{\rho c_s^2} (\nabla^C p + C \nabla^C \mu) \right]. \end{aligned} \quad (21)$$

Equation (1) recovers the following macroscopic equations [23]:

$$\frac{\partial p}{\partial t} + \rho c_s^2 \nabla \cdot \mathbf{u} = 0, \quad (22)$$

$$\rho \left(\frac{\partial \mathbf{u}}{\partial t} + \mathbf{u} \cdot \nabla \mathbf{u} \right) = -\nabla p - C \nabla \mu + \nabla \cdot \mathbf{\Pi}, \quad (23)$$

where $\mathbf{\Pi}$ is the viscous stress tensor. Also, the Cahn-Hilliard equation is recovered from Eq. (20) [23]:

$$\frac{\partial C}{\partial t} + \mathbf{u} \cdot \nabla C = M \nabla^2 \mu. \quad (24)$$

The macroscopic properties are related to the distribution functions by

$$C = \sum_{\alpha=0}^8 \bar{h}_\alpha, \quad (25)$$

$$p = \sum_{\alpha=0}^8 \bar{g}_\alpha + \frac{\delta_t}{2} \mathbf{u} \cdot \nabla^C \rho c_s^2, \quad (26)$$

$$\mathbf{u} = \frac{1}{\rho c_s^2} \left(\sum_{\alpha=1}^8 \bar{g}_\alpha \mathbf{e}_\alpha - \frac{\delta_t}{2} C \nabla^C \mu \right). \quad (27)$$

The density is taken as a linear function of the composition:

$$\rho = C \rho_l + (1 - C) \rho_g, \quad (28)$$

where ρ_l and ρ_g are the bulk densities of liquid and gas phases, respectively.

III. NUMERICAL RESULTS

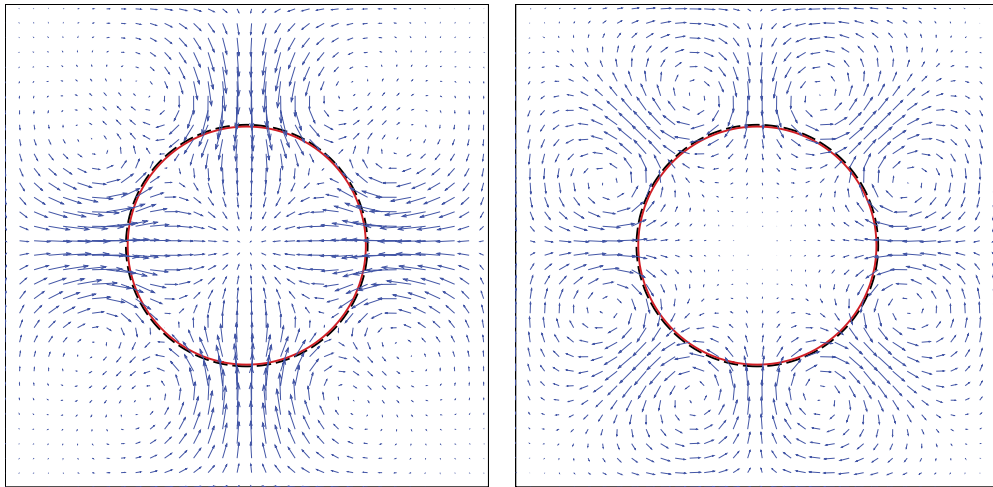
A. Parameter setup

The diagonal relaxation matrix in this study is chosen such that

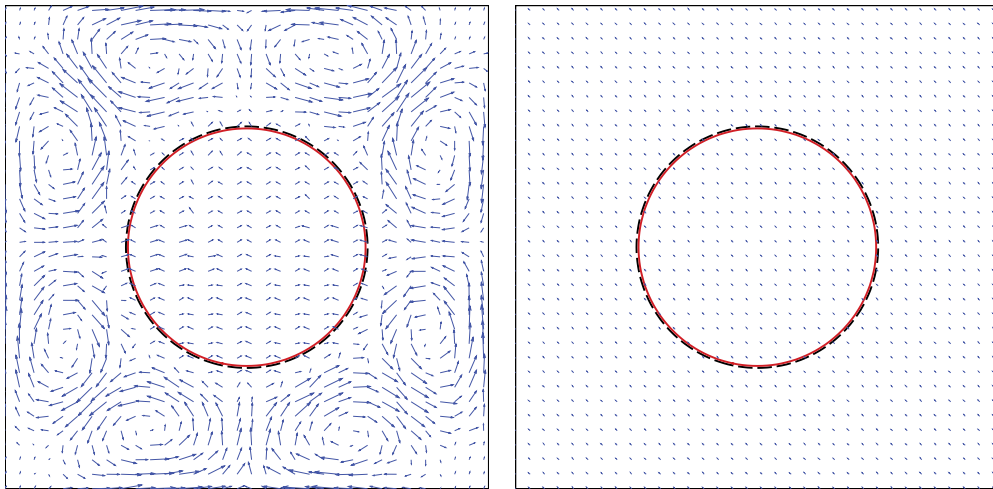
$$\hat{\mathbf{S}} = \text{diag}(0, 1, 1, 0, 1, 7, 0, 1, 7, s_8, s_8), \quad (29)$$

in which s_8 is related to the single relaxation time, and therefore the kinematic viscosity, by

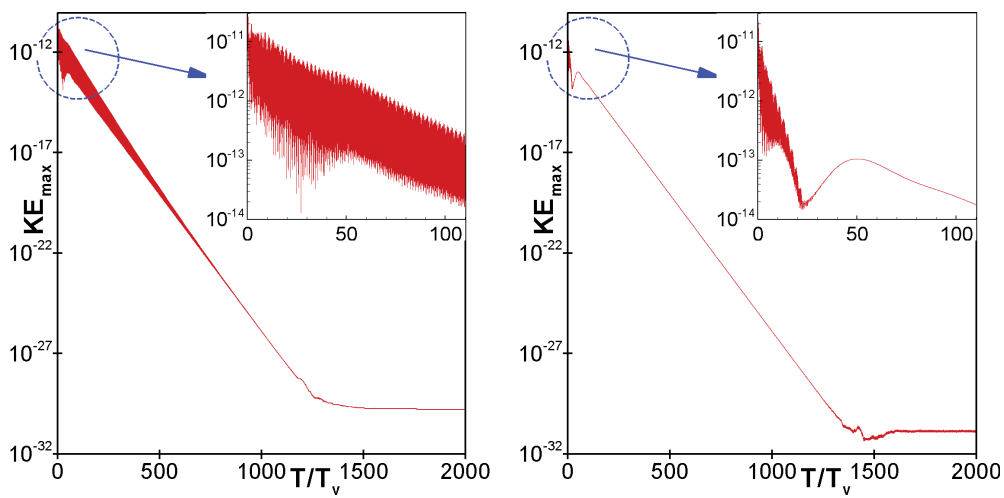
$$s_8 = \frac{1}{\tau + 0.5}, \quad \nu = \tau c_s^2. \quad (30)$$



(a) Spurious currents magnified by 10^7 at $T/T_v=100$. Left: BGK; right: MRT



(b) Spurious currents magnified by 10^{15} at $T/T_v=2000$. Left: BGK; right: MRT



(c) Maximum kinetic energy density versus dimensionless time. Left: BGK, right: MRT

FIG. 1. (Color online) A static droplet test with $\gamma = 0.0001$, $\tau = 0.03$, $\rho_g = 0.1$, and $\rho_l = 1$.

The dimensionless relaxation time τ in our model is different from the usual relaxation time by -0.5 , and thus, the minimum

value of τ is 0. This facilitates the interpolation of τ as an inverse linear function of the composition to get a monotonic

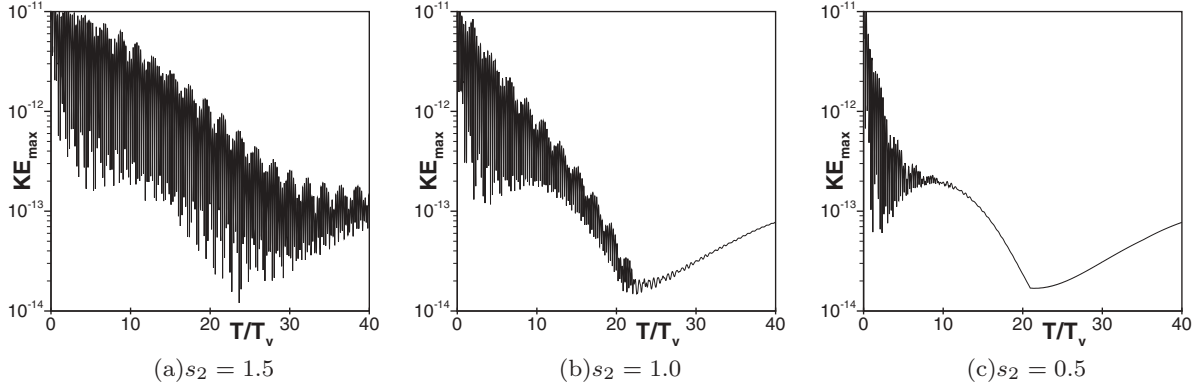


FIG. 2. Evolution of the maximum kinetic energy of the flow field at early times.

profile of the dynamic viscosity across the phase interface [23]. We have

$$\frac{1}{\tau} = \frac{C}{\tau_l} + \frac{(1 - C)}{\tau_g}, \quad (31)$$

where τ_l and τ_g are the bulk relaxation times of liquid and gas phases, respectively.

B. Spurious currents

A circular drop with an initial radius $R = 25$ in lattice unit is placed at the center of a periodic domain with 101×101 grid points, and the maximum kinetic energy density of the fluid is measured using both the BGK and MRT models. The input parameters are the same as those used in [29], except for the lower relaxation time in the present study. The gas and liquid densities are $\rho_g = 0.1, \rho_l = 1$, and $\tau = 0.03, \gamma = 0.0001$, and $\xi = 4$. The time T is made dimensionless using the viscous time $T_v = \eta_g R / \gamma$, with η_g being the dynamic viscosity of the gas phase. The spurious currents at $T/T_v = 100$ and $T/T_v = 2000$ are shown in Fig. 1, together with the evolution of the maximum kinetic energy in the flow versus time.

Previously [29], we have shown that given the interface thickness, density ratio, viscosity, and surface tension, faster convergence toward the equilibrium state can be achieved via stronger mobility and elimination of traveling waves caused by the dynamic pressure. In Fig. 1, both the BGK and MRT models are capable of eliminating the spurious currents to the machine precision, and their convergence rates are nearly identical. It is noteworthy, however, that the MRT model is successful at damping high-frequency oscillations in the kinetic energy emerging from the traveling waves generated by the inclusion of curvature at early times, whereas the oscillations tend to persist in the BGK model as clearly demonstrated in Fig. 1(c). These high-frequency oscillations at the initial stages, which appear to contribute to the numerical instability of BGK models, become more pronounced as the relaxation time decreases. The implication of this rapid damping of the traveling waves is not trivial as the convergence toward the equilibrium state is hardly achieved in most transient flow calculations. The major parameter that controls these oscillations is s_2 . This is rather expected since s_2 is the relaxation time associated with the energy mode [22], and under-relaxing s_2 allows the energy mode to relax to

its equilibrium state faster, as shown in Fig. 2. However, it should not be interpreted that having a low relaxation rate for s_2 is always the optimum choice for stability. In our Kelvin-Helmholtz instability simulations, we obtained more stable results by setting s_2 equal to 1.

C. Kelvin-Helmholtz instability for a single-phase fluid

In this section, temporal growth of an initially small disturbance in the form of a cosine wave is examined and the results are compared with the recent study by Fontane and Joly [13]. The dimensionless velocity profile across the shear layer consists of a base flow and small perturbations for initiation of KHI:

$$\begin{aligned} u(y) &= \tanh\left(\frac{y}{\delta}\right) + \varepsilon u'(y) \cos(\alpha x) \\ v(y) &= \varepsilon v'(y) \cos(\alpha x), \end{aligned} \quad (32)$$

where δ is half the shear-layer depth or vorticity thickness, $\alpha = 2\pi/\lambda$ is the wave number with λ being the wavelength, ε is the perturbation amplitude, and u' and v' are the complex eigenfunctions of the Rayleigh stability equation [2,30]. Inviscid stability analysis is carried out to determine these eigenfunctions [30]. For the most unstable mode, we found $\alpha\delta = 0.44492$.

We seed the initial disturbances similar to [13]. The computations are performed in a 256×257 grid with the periodicity of λ in the streamwise direction and free-slip boundary condition at the top and bottom boundaries. The Reynolds number of the flow is defined as

$$Re = \frac{U_0 \delta}{\nu}, \quad (33)$$

where U_0 is half the velocity difference across the shear layer. The surface tension is neglected and the dimensionless time is defined by $t = T U_0 / \delta$.

The comparison between the performance of the BGK and MRT models is made in Fig. 3. Wiggles start to emerge in the vorticity contour for the BGK model at $Re = 2000$ in Fig. 3(a), and they completely overshadow the vorticity contours at $Re = 2500$ in Fig. 3(b). On the other hand, the MRT model successfully captures the Kelvin-Helmholtz billows in Fig. 3(c). A similar observation was made by Dellar [31], who attributed the enhanced stability of the MRT model to

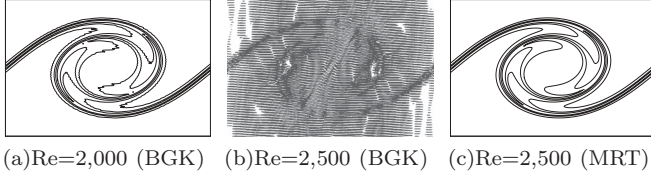


FIG. 3. Vorticity contours for single-phase flow at $t = 26$ (dimensionless contour increment is $1/6$).

the increased bulk viscosity. Utilizing the MRT model, we could reach a Reynolds number as high as 100,000 at which the wiggles start to appear. The current MRT model is also compared with the AMR approach by Fontane and Joly [13], and the results are illustrated in Fig. 4. As it is seen, the MRT results are in good agreement with those reported in [13].

D. Kelvin-Helmholtz instability of two immiscible fluids

The majority of the previous studies on KHI dealt with two miscible fluids utilizing the Boussinesq approximation, and a few works have been done for immiscible fluids with a density contrast. Most of the published papers did not take into account either the effects of density ratio or surface tension, and some of them only considered inviscid fluids. One of the aims of this study is to fill this gap by investigating the effects of density, viscosity, and surface tension especially at high Reynolds numbers. Following Cenicerros and Roma [12], we choose four dimensionless groups for describing the physics of the problem: density ratio, viscosity ratio, Reynolds number

$$\text{Re} = \frac{U\lambda}{\nu_g}, \quad (34)$$

and Weber number

$$\text{We} = \frac{\rho_g U^2 \lambda}{\gamma}, \quad (35)$$

where ν_g is the kinematic viscosity of the gas phase and $U = 2U_0$ is the reference velocity in accordance to Refs. [11,12]. As a diffuse interface approach, LBM requires an additional parameter, the Péclet number

$$\text{Pe} = \frac{U\lambda}{M\beta}. \quad (36)$$

Also, the dimensionless time is defined by $t = UT/\lambda$.

First we compare our results with those of the AMR scheme [12] for density-matched fluids. We prescribe a vortex sheet in a similar way as specified in [12]. Initially, the

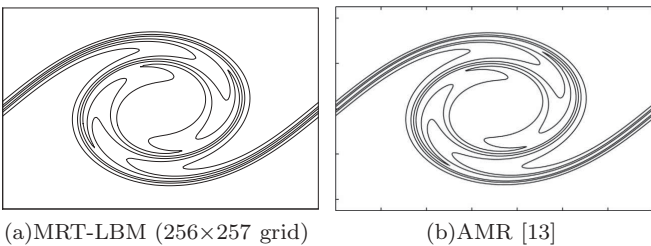


FIG. 4. Single-phase Kelvin-Helmholtz billows with $\text{Re} = 1500$ at $t = 26$ (dimensionless contour increment is $1/6$).

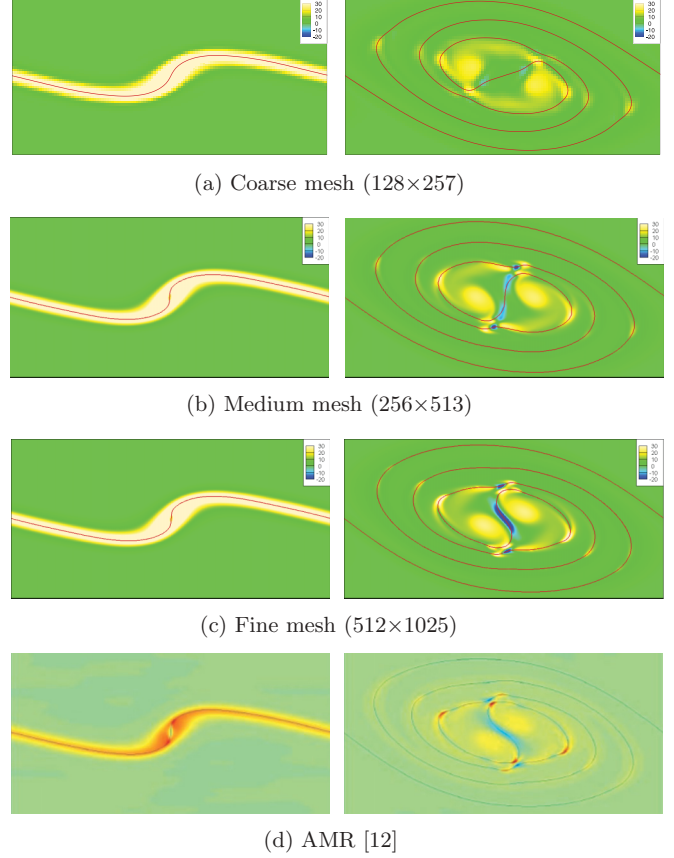


FIG. 5. (Color) Vorticity contour and interface location (red line) for $\text{Re} = 5000$, $\text{We} = 400$, $\text{Pe} = 1000$, and $\xi = 3$. Left: $t = 0.7$, right: $t = 3.5$.

interface is perturbed with a uniformly concentrated vorticity distribution in a domain of size $(\lambda \times 2\lambda)$. The interface location in dimensionless form is given by

$$\phi(x, y) = \frac{y}{\lambda} + 0.01 \sin\left(\frac{2\pi(x+y)}{\lambda}\right). \quad (37)$$

The vorticity is a Dirac δ function concentrated at the interface:

$$\omega_0(x, y) = \delta_h(\phi(x, y)). \quad (38)$$

Invoking a sharp interface approach, Cenicerros and Roma [12] approximated the δ function with a cosine function. Here we adopt a smoothed version of the cosine function [32]:

$$\delta_h(\phi) = \begin{cases} \frac{\pi + 2 \sin[\pi(2\phi+1)/4] - 2 \sin[\pi(2\phi-1)/4]}{4\pi}, & |\phi| < 1.5 \\ \frac{5\pi - 2\pi|\phi| - 4 \sin[\pi(2|\phi|-1)/4]}{8\pi}, & 1.5 \leq |\phi| \leq 2.5 \\ 0, & 2.5 < |\phi|. \end{cases} \quad (39)$$

Initially, the upper wall has a slip velocity of U_0 to the left while the lower wall is moving to the right with U_0 . To reduce the compressibility effects as much as possible, the Mach number $\text{Ma} = U_0/c_s$ of the density-matched flow is set to 0.026.

First, the grid convergence is verified on three different systematically refined grids and the vorticity contours are compared with the AMR results [12] for $\text{Re} = 5000$ in Fig. 5 and for $\text{Re} = 10,000$ in Fig. 6. The Weber number is 400 and the Péclet number and the interface thickness are fixed

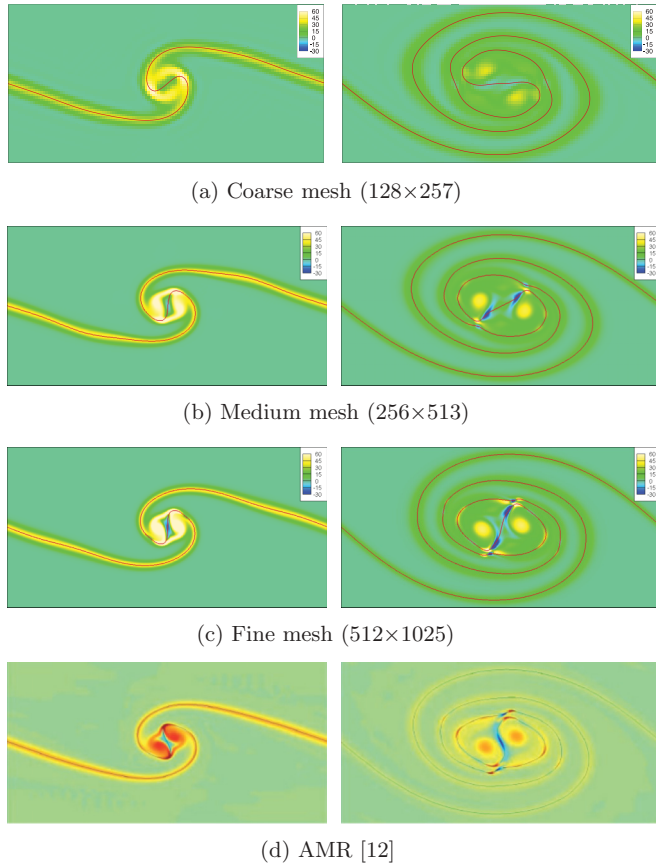


FIG. 6. (Color) Vorticity contours and interface location (red line) for $Re = 10,000$, $We = 400$, $Pe = 1000$, and $\xi = 3$. Left: $t = 1.0$, right: $t = 2.5$.

at $Pe = 1000$ and $\xi = 3$, respectively. As can be seen in Figs. 5 and 6, the contour plots of vorticity and density are approaching the AMR results as the grid resolution increases. While satisfactory results are obtained with the moderate size 256×513 grid, the MRT simulations on the finest grid (512×1025) are in better agreement with those using AMR technique. The symmetric interface rollup is accurately predicted using both moderate and fine grids. Hence, most of the simulations are carried out in a domain with the moderate grid unless the need for a finer mesh is anticipated.

We continue with our simulations of shear-layer instability of two immiscible fluids with different densities. In this part, the initial velocity is chosen such that the Mach number is equal to 0.05. Figure 7 shows the temporally growing mixing layer at different density ratios and moderate Reynolds numbers. We can observe the generation of a small wave at the interface with a thick tip for $Re = 200$. As the Reynolds number increases, the tip stretches into a narrow ligament of liquid with a thin tip. This long finger of interpenetrating fluids is also observed in the previous studies [11,12]. At high enough Reynolds numbers in Fig. 8, a small ligament is detached from the liquid phase. However, for the density-matched fluids we do not see any breakup pattern. The reason for the chaotic breakup of the interface at higher Reynolds numbers in Fig. 8 becomes clear as one considers the Reynolds number of the liquid. As the density ratio increases, inertial forces in the

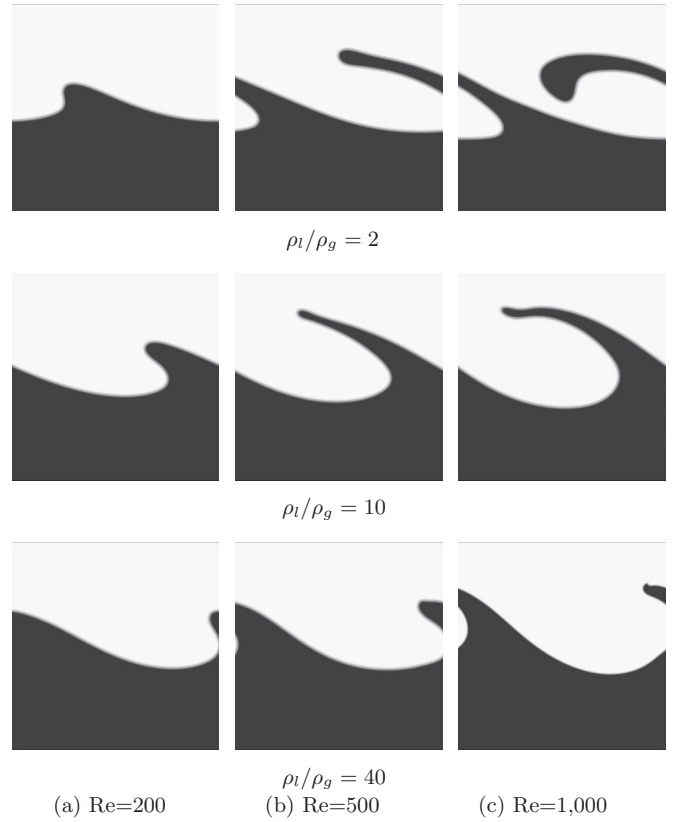


FIG. 7. Snapshots of KHI at different density ratios and moderate Reynolds numbers ($\eta_l/\eta_g = 10$, $We = 400$, $\xi = 4$, $t = 3.5$).

liquid are more dominant than viscous forces, causing a highly deformed interface and eventually catastrophic breakup of the interface. On the other hand, we notice the flow field is no longer symmetric for two fluids with different densities. This asymmetry of the interface topology as the density ratio increases was also reported by Tauber *et al.* [11]. It should be mentioned that the computations in Fig. 7(c) for $\rho_l/\rho_g = 40$,

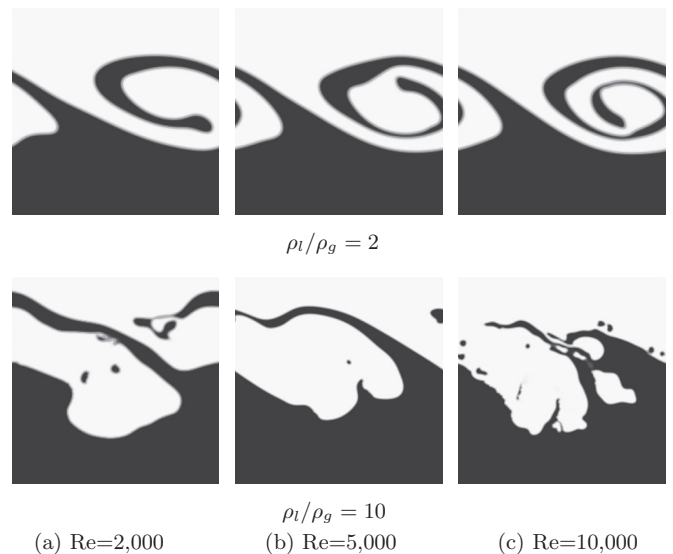


FIG. 8. Snapshots of KHI at higher Reynolds numbers ($\eta_l/\eta_g = 10$, $We = 400$, $\xi = 4$, $t = 3.5$).

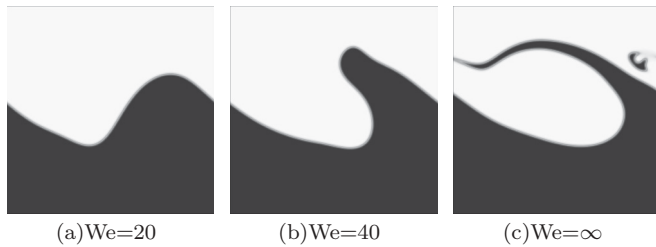


FIG. 9. Effect of Weber number ($\rho_l/\rho_g = 10$, $\eta_l/\eta_g = 10$, $Re = 2000$, $\xi = 4$, $t = 3.5$).

and in Figs. 8(b) and 8(c) for $\rho_l/\rho_g = 10$ are performed using a fine (512×1025) grid, because the results for the moderate grid were found to be under-resolved.

The stabilizing effect of surface tension is demonstrated in Fig. 9 for $Re = 2000$. Lower Weber numbers result in a more stable phase interface and prevent the interface pinch-off. We observe a well-shaped wave at the interface in Fig. 9(a). As the Weber number increases, the wave elongates further and its tip gets narrower, and finally, interface pinch-off is observed in the absence of surface tension in Fig. 9(c).

It is worth noting that the contour plots of concentration shown in Figs. 7–9 span from 0.1 to 0.9 with an increment of 0.1. As it is seen in these figures, the interface thickness remains within the prescribed value of $\xi = 3\text{--}5$ lattice units.

IV. SUMMARY AND CONCLUSION

A consistent version of the MRT-LBM for immiscible multiphase flows, in the sense that the relaxation matrix can be applied in the same manner as the single-phase MRT-LBM, was developed and verified for its accuracy and stability. The Kelvin-Helmholtz instability of immiscible two-phase fluids was investigated, and comparison of the results with prior AMR studies at high Reynolds numbers was made. It is found that the Reynolds number is the most important factor in stabilizing/destabilizing the interface. On the other hand, a finger of interpenetrating fluids is observed at low surface tension values. As the interfacial force is increased, the length of the finger is shortened and at a high enough surface tension the interface roll-up is completely suppressed. A convoluted interface in the shape of a spiral was observed for two fluids with the same density and viscosity. At low Reynolds numbers, increasing the density ratio turns the interface deformation into a standing capillary wave shape. For higher Reynolds numbers, increasing the density ratio destabilizes the flow field, turning the interface into a highly deformed thin finger of interpenetrating fluids with an asymmetric structure.

ACKNOWLEDGMENTS

This research is being performed using funding received from the DOE’s NEUP. A.F. would like to thank Charles Maldarelli for insightful discussions.

[1] S. Chandrasekhar, *Hydrodynamic and Hydromagnetic Stability* (Clarendon Press, Oxford, 1961).

[2] A. Michalke, *J. Fluid Mech.* **19**, 543 (1964).

[3] P. Hazel, *J. Fluid Mech.* **51**, 39 (1972).

[4] P. C. Patnaik, F. S. Sherman, and G. M. Corcos, *J. Fluid Mech.* **73**, 215 (1976).

[5] R. W. Metcalfe, S. A. Orszag, M. E. Brachet, S. Menon, and J. J. Riley, *J. Fluid Mech.* **184**, 207 (1987).

[6] R. H. Rangel and W. A. Sirignano, *Phys. Fluids* **31**, 1845 (1988).

[7] G. P. Klaassen and W. R. Peltier, *J. Fluid Mech.* **227**, 71 (1991).

[8] R. D. Moser and M. M. Rogers, *J. Fluid Mech.* **247**, 275 (1993).

[9] C. Staquet, *J. Fluid Mech.* **295**, 73 (1995).

[10] C. P. Caulfield and W. R. Peltier, *J. Fluid Mech.* **413**, 1 (2000).

[11] W. Tauber, S. O. Unverdi, and G. Tryggvason, *Phys. Fluids* **14**, 2871 (2002).

[12] H. D. Cenicerros and A. M. Roma, *Phys. Fluids* **16**, 4285 (2004).

[13] J. Fontane and L. Joly, *J. Fluid Mech.* **612**, 237 (2008).

[14] M. S. Shadloo and M. Yildiz, *Int. J. Numer. Meth. Engng.* **87**, 988 (2011).

[15] X. He and L.-S. Luo, *Phys. Rev. E* **56**, 6811 (1997).

[16] S. Chen and G. D. Doolen, *Annu. Rev. Fluid Mech.* **30**, 329 (1998).

[17] R. Zhang, X. He, G. D. Doolen, and S. Chen, *Adv. Water Res.* **24**, 461 (2001).

[18] X. He, X. Shan, and G. D. Doolen, *Phys. Rev. E* **57**, R13 (1998).

[19] X. He, S. Chen, and R. Zhang, *J. Comput. Phys.* **152**, 642 (1999).

[20] P. L. Bhatnagar, E. P. Gross, and M. Krook, *Phys. Rev.* **94**, 511 (1954).

[21] Y. H. Qian, D. d’Humières, and P. Lallemand, *Europhys. Lett.* **17**, 479 (1992).

[22] P. Lallemand and L.-S. Luo, *Phys. Rev. E* **61**, 6546 (2000).

[23] T. Lee and L. Liu, *J. Comput. Phys.* **229**, 8045 (2010).

[24] T. Lee and C.-L. Lin, *J. Comput. Phys.* **206**, 16 (2005).

[25] M. E. McCracken and J. Abraham, *Phys. Rev. E* **71**, 036701 (2005).

[26] A. Fakhari and M. H. Rahimian, *Phys. Rev. E* **81**, 036707 (2010).

[27] A. Fakhari and M. H. Rahimian, *Comp. Fluids* **40**, 156 (2011).

[28] H. Ding, P. D. M. Spelt, and C. Shu, *J. Comput. Phys.* **226**, 2078 (2007).

[29] T. Lee, *Comp. Math. Appl.* **58**, 987 (2009).

[30] W. D. Smyth, J. N. Moum, and J. D. Nash, *J. Phys. Oceanography* **41**, 412 (2011).

[31] P. Dellar, *J. Comput. Phys.* **190**, 351 (2003).

[32] X. Yang, X. Zhang, Z. Li, and G.-W. He, *J. Comput. Phys.* **228**, 7821 (2009).